Barotropic and Baroclinic Tides in the Central North Pacific Ocean Determined from Long-Range Reciprocal Acoustic Transmissions

BRIAN D. DUSHAW,* BRUCE D. CORNUELLE,** PETER F. WORCESTER,** BRUCE M. HOWE,* AND DOUGLAS S. LUTHER[‡]

*Applied Physics Laboratory, College of Ocean and Fishery Sciences, University of Washington, Seattle, Washington
**Scripps Institution of Oceanography, University of California, San Diego, La Jolla, California
[‡]Department of Oceanography, School of Ocean and Earth Science and Technology, University of Hawaii at Manoa, Honolulu, Hawaii

ABSTRACT

Travel times of reciprocal 1000-km range acoustic transmissions, determined from the 1987 Reciprocal Tomography Experiment, are used to study barotropic tidal currents and a large-scale, coherent baroclinic tide in the central North Pacific Ocean. The difference in reciprocal travel times determines the tidal currents, while the sum of reciprocal travel times determines the baroclinic tide displacement of isotachs (or equivalently, isotherms). The barotropic tidal current accounts for 90% of the observed differential travel time variance. The measured harmonic constants of the eight major tidal constituents of the barotropic tide and the constants determined from current meter measurements agree well with the empirical–numerical tidal models of Schwiderski and Cartwright et al. The amplitudes and phases of the first-mode baroclinic tide determined from sum travel times agree with those determined from moored thermistors and current meters. The baroclinic tidal signals are consistent with a large-scale, phase-locked internal tide, which apparently has propagated northward over 2000 km from the Hawaiian Ridge. The amplitude, phase, and polarization of the first-mode M_2 baroclinic tidal displacement and current are consistent with a northward propagating internal tide. The ratio of baroclinic energy to barotropic energy determined using the range-averaging acoustic transmissions is about 8%, while a ratio of 26% was determined from the point measurements. The large-scale, internal tide energy flux, presumed northward, is estimated to be about 180 W m^{-1}.

1. Introduction

Tidal effects on long-range acoustic transmissions have been reported by Weinberg et al. (1974), Munk et al. (1981), Headrick et al. (1993), and Dushaw et al. (1994, hereafter DWCHc). Munk et al. (1981) reported the observed tidal variations from several one-way transmission experiments in the western North Atlantic and reviewed the possible tidal effects on long-range transmissions. They found that the observed tidal variations in acoustic travel times could be explained as a combination of the barotropic tides, baroclinic tides, and motion of the moored acoustic instruments, depending on the experiment considered. Howe et al. (1987) were unable to observe the barotropic tidal currents from reciprocal transmissions at 300-km range in the western North Atlantic because the acoustic path was oriented along the minor (very small) tidal axis. Headrick et al. (1993) reported the tidal signals observed in five 4000-km long, one-way transmissions from Hawaii to the west coast of North America. They found that a model for barotropic tidal currents, based

on Schwiderski's empirical–numerical tidal elevation maps (Schwiderski 1980, hereafter Schwiderski), could account for the observed tidal signals on three of the acoustic paths, but invoked seamount-generated internal tides to explain discrepancies on two paths. DWCHc, using the reciprocal travel time data from the 1987 Reciprocal Tomography Experiment (RTE87), verified that barotropic tidal currents could be accurately determined from reciprocal transmissions. Barotropic tidal harmonic constants determined acoustically in this experiment agreed with those determined from moored current meters and the empirical–numerical models of Schwiderski and of Cartwright et al. (1992, hereafter CRS).

In this paper, we discuss measurements of both baroclinic and barotropic tides using reciprocal acoustic transmissions over paths 1000 km long in the central North Pacific Ocean during summer 1987. We are concerned here with understanding the high-frequency variability (>1 cpd) of travel times. The acoustically observed, low-frequency current and temperature variability has already been reported by Dushaw et al. (1993b, hereafter DWCHb) and DWCHc.

DWCHc have previously reported the barotropic tides determined acoustically on the north leg of RTE87. In this paper, the results for the other two ex-

Corresponding author address: Dr. Brian D. Dushaw, Applied Physics Laboratory, University of Washington, 1013 NE 40th Street, Seattle, WA 98105-6698.

periment legs are given and the method of deriving the tidal components from the barotropic currents is discussed in greater detail. A comparison of the measured and modeled harmonic constants of the eight major tidal constituents along all three legs shows that the Schwiderski and CRS models determine tidal current with satisfactory agreement.

The acoustic data reported here contain the signal of a large-scale, phase-locked internal tide. We suggest that the observed internal tide has propagated over 2000 km from the Hawaiian Ridge. The observation of this large-scale internal tide likely results from the quiescent nature of the central North Pacific Ocean (Emery 1983; Shum et al. 1990; DWCHb), the sensitivity of the acoustic measurements to isotach (lines of constant sound speed) displacements, and the suppression relative to point temperature and current measurements of internal wave noise in the acoustic measurements. The acoustical array acts as a highly directive antenna for the incident internal tide. The observations imply that the internal tide field is a superposition of a dominant, narrowband, stochastic process and a large-scale, coherent wave.

It is commonly assumed that midocean internal tides have correlation lengthscales of order 100–200 km (Wunsch 1975; Munk et al. 1981) and are not phase locked to the barotropic tides except for locally forced internal tides. Wunsch (1975) stated: "It is difficult to believe that waves of such small scale (wavelengths of 100–200 km) will be able to transmit 'knowledge' of boundaries across thousands of kilometers in the presence of advecting currents and dissipation." Currents can cause the baroclinic tide to be spatially distorted and the baroclinic tidal frequencies to be shifted from the astronomical tidal frequencies. On the other hand, some theoretical considerations suggest that the lowest-mode internal tide propagates thousands of kilometers before dissipating (LeBlond 1966; Schott 1977; LeBlond and Mysak 1978). A far-field internal tide was reported by Hendry (1977), who used data from the Mid-Ocean Dynamics Experiment (MODE) in the western North Atlantic Ocean to show that a deterministic semidiurnal internal tide propagated about 720 km from the Blake Escarpment.

An important and unresolved problem is the rate of energy loss of the barotropic tide to the baroclinic tide (Wunsch 1975; Hendershott 1981). Using the present internal tide observations, the ratio of baroclinic to barotropic tidal energy is discussed. Since the acoustic measurements represent a range average of the internal tidal perturbation, not the squared perturbation, only a lower bound on the ratio of baroclinic to barotropic tidal energy can be determined from them. The energy ratio determined at one point using thermistors and current meters is three times that determined acoustically.

In section 2, the data are described and the tidal signature in the travel times is shown. In section 3 the

barotropic tidal currents are estimated. In section 4, the theoretical description of the internal tide is briefly reviewed. The dynamical and kinematic equations describing the baroclinic tide are then applied to the acoustical data. The acoustical results are compared with the tidal results from moored thermistors and current meters located on one of the acoustic paths. In section 5, the barotropic and baroclinic tidal energies are discussed. In section 6, the variability of the acoustic travel times due to nontidal internal waves is discussed. Finally, in section 7, we present our conclusions.

2. Data

The 1987 Reciprocal Tomography Experiment was a 4-month long experiment, previously described by Dushaw et al. (1993a, hereafter DWCHa), DWCHb, DWCHc, and Worcester et al. (1990, 1991), which consisted of three moored broadband acoustic transceivers separated by 745, 995, and 1275 km (Fig. 1). Transmissions were made bihourly on every fourth day. The data collected consisted of travel times of acoustic pulses associated with identified ray paths. The transceivers in this experiment were located near the sound channel axis at about 900 m. Only deep-turning, surface-reflected (or near-surface refracted) rays and an axial ray (the ray that remains near the sound channel axis) were resolved (Fig. 2). The axial ray corresponds to the slowest acoustic energy. The measured travel times have been corrected for clock error and mooring motion (DWCHa).

Currents and sound speed perturbations can be estimated from the sum and the difference of reciprocal travel times (DWCHc have verified that the raypaths of reciprocal transmissions are sufficiently identical to permit such combinations of travel times). To first order in $\delta c / c$ and $\mathbf{u} \cdot \boldsymbol{\tau} / c$ (DWCHb,c)

$$T_i^+(t) - T_i^-(t) \approx -2 \int_{\Gamma_i} \frac{\mathbf{u}(\mathbf{x}, t) \cdot \boldsymbol{\tau}}{c_0^2(\mathbf{x})} \, ds, \quad (1)$$

and

$$T_i^+(t) + T_i^-(t) \approx 2 T_{0i} - 2 \int_{\Gamma_i} \frac{\delta c(\mathbf{x}, t)}{c_0^2(\mathbf{x})} \, ds, \quad (2)$$

where T_i^+ and T_i^- are the reciprocal travel times for ray path Γ_i, $c_0(\mathbf{x})$ is a reference sound-speed field, $\delta c(\mathbf{x}, t)$ is the perturbation in sound speed, $\mathbf{u}(\mathbf{x}, t)$ is the current, $\boldsymbol{\tau}$ is the direction of the ray path, ds is an increment of arc length, t is time (yearday), and

$$T_{0i} = \int_{\Gamma_i} \frac{ds}{c_0(\mathbf{x})}. \quad (3)$$

It is not possible to determine a spectrum from these travel-time series in the usual way because of the nonuniform sample intervals. A tidal signal is evident in both the sum and the difference travel times (Figs. 3 and 4), however, and weighted least squares techniques
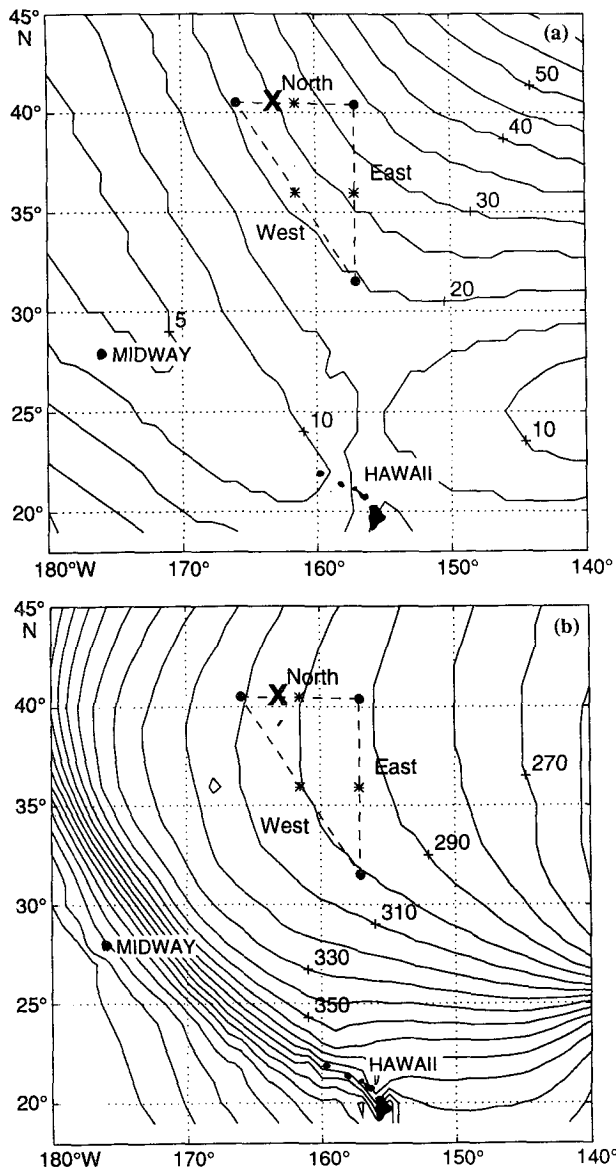
FIG. 1. Geometry of the 1987 gyre-scale reciprocal tomography experiment. Panel (a) shows M_2 amplitude lines in centimeters and (b) shows M_2 cotidal lines in degrees. The acoustic transceivers are located at the circles. The location of the current meter mooring is marked by X. The locations for which results of the Schwiderski numerical tide model are given are denoted by stars. North, East, and West are the names given to the legs of the triangle. The triangle is located north of Hawaii between the subtropical and subarctic fronts. (Modified from Schwiderski 1979.)

will be used to extract these signals. The sum travel times in this paper are high-pass filtered (>1 cpd) by removing the daily average (more complicated filters are not possible because of the sampling strategy). The differential travel times are dominated by tidal current and contain no trends, hence they are left unfiltered. While tidal fluctuations of the axial and deep-turning ray differential travel times are similar magnitude, the

tidal fluctuations of the sum travel times for the axial ray are much larger than those of the deep-turning rays. Figure 2 shows that the axial ray turns at depths that are near the maximum of the first baroclinic (sound speed) mode, while the deep-turning rays turn at depths for which the baroclinic sound speed perturbations are small. A least squares tidal analysis applied to the travel times of each ray path separately gives an M_2 *current* amplitude of 1.28 cm s^{-1} (1.18 cm s^{-1}) for the deep-turning (axial) rays (and the same phase), while the M_2 *sound speed* perturbation amplitude is 0.85 cm s^{-1} (4.06 cm s^{-1}) for the deep-turning (axial) rays (and the same phase). This suggests that the main tidal signal in the differential travel times is due to the barotropic tidal current, while the tidal signal in the sum travel times is due to the baroclinic tidal perturbation of the isotach lines. This analysis will be done more consistently below, when linear inverse techniques are used to combine the data from all the ray paths to solve for the sound speed and current perturbations caused by the tides.

The noise in the travel times, evident in Figs. 3 and 4, is attributed to internal wave–induced travel time variability (in this paper "internal waves" are distinguished from the "internal tide"), since the measurement uncertainty of the sum travel times is only a few milliseconds (DWCHa) (dominated by the mooring position uncertainty). The measurement uncertainty of the differential travel times is about one millisecond (DWCHc). The rms internal wave noise is used as the data uncertainty for the purposes of the inversions for current and sound speed. Separation of the tidally induced travel time variability from the internal wave–induced travel time variability is an iterative problem, since to extract the tidal signal using weighted least squares requires assuming a noise level that cannot be checked until the tides are removed. This will be discussed further in section 3.

The acoustic data are complemented by a subsurface mooring with current meters and thermistors located at 40.647°N, 163.025°W, midway along the northern transmission path (Fig. 1). Current meters and thermistors were located at depths of 73, 173, 946, 2498, 5650, and 5722 m, with an additional thermistor at 296 m. Vector-averaged current and averaged temperature measurements were recorded every half hour for one year. Much of the variability of the temperature and current measurements is due to internal waves. DWCHc found that the barotropic tide accounted for 90% of the variance of the unfiltered, acoustically determined barotropic current, but only 25% of the variance of the unfiltered current meter–determined barotropic current. Luther et al. (1991) reported that weak currents caused frequent stalling of the deep current meters, which forced artificial (but independently corroborated) corrections to the current meter data. The three deepest thermistors suffered similar "stalling" caused by insufficient dynamic range settings, and so
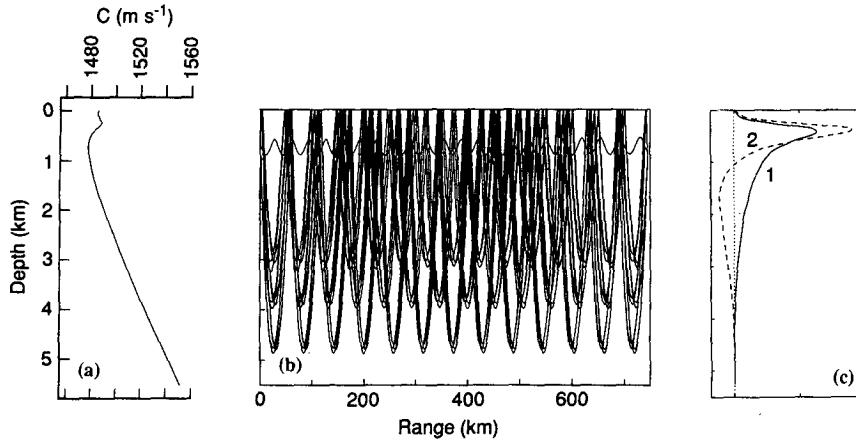
FIG. 2. (a) Sound speed profile and (b) ray paths for the north leg of the triangle. Only resolved ray paths are shown, and the path for the slowest acoustic energy is represented as the axial ray near 800-m depth. Panel (c) shows the first two internal tide sound speed modes. The axial ray travels in the region where the baroclinic modes are largest. (Modified from Worcester et al. 1991.)

are not used here. The tidal signal-to-noise ratio is much better for the acoustic data than for the moored data, but the moored data nonetheless usefully corroborate the acoustic results.

3. Barotropic tides

In this section we report barotropic tidal current harmonic constants determined from the acoustic

travel times, compare those constants with current meter estimates, and examine the accuracy of empirical–numerical tidal models. The current meter determination of barotropic and baroclinic currents and the tidal analysis technique used to estimate the harmonic
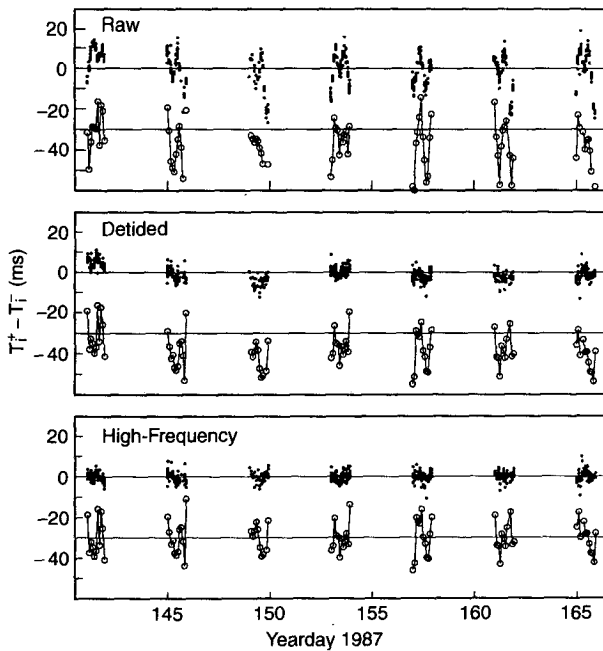

FIG. 3. The raw, detided, and high-frequency (>1 cpd) differential travel times for the first few days of the time series on the north leg. Dots are data from the deep-turning rays. Open circles are data from the axial ray that have been offset by 30 ms. Comparing the axial and deep-turning ray travel times suggests that the tidal variability is barotropic. (Modified from DWCHa.)
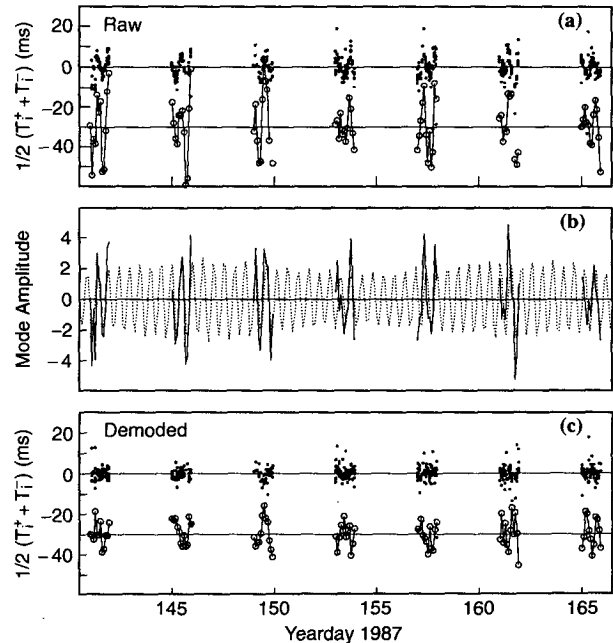
FIG. 4. Panel (a) shows the raw high-frequency (>1 cpd) sum travel times for the first few days of the time series on the north leg. Dots are data from the deep-turning rays. Open circles are data from the axial ray that have been offset by 30 ms. Panel (b) shows the time series of the amplitude of the first internal tide mode (solid line) extracted from the time series of (a). The dotted line shows the deterministic tidal signal from the fit to the time series of mode amplitudes. Panel (c) shows the residual of the sum travel times after the modal signature has been removed.

constants are described. In section 4 the tidal analysis technique is also used to estimate the harmonic constants of the first-mode baroclinic-tide temperature and current signals.

a. Acoustical observations

The differential travel times are well suited to determining the large-scale, barotropic tidal currents. Since the measurements are inherently range and depth averaging, the horizontal and vertical structure of the baroclinic tidal currents means that baroclinic tidal energy is suppressed relative to the barotropic tidal energy in the differential travel times. This conclusion is supported by the similarity of the axial and deep-turning ray differential travel-time series. We proceed on the assumption that the baroclinic currents negligibly alias into the acoustically determined barotropic currents and verify this assumption in section 4.

We have used inverse methods in (1) to solve for the barotropic (depth averaged) current from the differential travel times. Since DWCHc described this procedure, it will not be repeated here. A weighted least square estimation procedure is used to determine the tidal harmonic constants of the barotropic current. The barotropic tidal current is represented as

$$U(t) = \sum_{N=1}^{8} A_N \cos(\omega_N t - \phi_N) + \epsilon(t), \qquad (4)$$

where the ω_N are the frequencies of the major tidal constituents (K_2, S_2, M_2, N_2, K_1, P_1, O_1, and Q_1), A_N and ϕ_N are the amplitude and phase, and $\epsilon(t)$ is noise. That the tidal constituent frequencies are exactly known can allow resolution of tidal harmonic constants, even if the signal-to-noise is low or if the record length is short (Munk and Hasselmann 1964). Equation (4) is more conveniently represented as

$$U(t) = \sum_{N=1}^{8} B_N \cos(\omega_N t) + \sum_{N=1}^{8} C_N \sin(\omega_N t) + \epsilon(t),$$
$$(5)$$

with

$$A_N = \sqrt{B_N^2 + C_N^2}, \quad \phi_N = \tan^{-1}\left(\frac{C_N}{B_N}\right). \qquad (6)$$

The weighted least squares technique [see the appendix for more details of the procedure which is also called the stochastic inverse (Aki and Richards 1980)] fits this representation of the tides to the acoustically determined barotropic currents and takes into account the uncertainty in the currents and a priori estimates of the magnitudes of B_N and C_N. Since the technique minimizes the norm of the solution, as well as the misfit, it is a biased estimator. The noise term is the combination of the uncertainty in the barotropic current estimates from the travel times and, predominantly,

nontidal current variance. Unweighted least squares (Zetler et al. 1965; Pugh 1987) are first employed to give initial estimates of the B_N, C_N, and nontidal variance. With these initial estimates, the biased estimator is then used to again estimate the B_N and C_N, together with the uncertainties. The final results for B_N and C_N are not sensitive to significant changes in the a priori assumptions.

The inverse method used here for the harmonic analysis of tides appears to be little used in the tidal literature, though it is often used for other applications. The weighted least squares approach is a modern inverse technique for estimating harmonic constants and their uncertainty, though it is only an incremental improvement over unweighted least squares. A least squares technique, rather than Fourier analysis, is required when the data are unequally spaced and when the record length is not a synodic period. The weighted least squares procedure is a natural extension of the approaches of Munk and Hasselmann (1964) and Zetler et al. (1965). Munk and Hasselmann showed that the resolution of the harmonic constants of two neighboring spectral lines is ultimately limited by the underlying noise in the data. They further showed that prior knowledge of the constituent frequencies could allow for a much greater resolution of the harmonic constants than would otherwise be possible. The unweighted least squares analysis is described by Pugh (1987) and is commonly used for tidal analysis (Perkins et al. 1994, for example). Both weighted and standard least squares analysis allow for misfit between the model and the data according to the prescribed data noise. Weighted least squares also takes into account prior expectations of the approximate amplitudes of the constituent frequencies and determines error bars that take into account data noise and cross-talk between the constituent frequencies. For example, if the data have a near-zero signal-to-noise ratio, weighted least squares will give nearly zero for the harmonic amplitudes with an uncertainty only slightly below the prior uncertainty in their values. If the weighting of model parameters becomes infinite, unweighted least squares is recovered and the error bars become smaller. The inverse could be further extended either to include known relationships between the constituent frequencies by enforcing correlations between those frequencies (in the matrix $\mathbf{R_{AA}}$ of the appendix) or to model the response to the equilibrium tide (together with a "credo of smoothness") as first described by Munk and Cartwright (1966). We have chosen not to use these extra assumptions, however, since the correct choices were not obvious.

b. Current meter observations

The harmonic constants are derived from the current meter measurements by two methods, since the estimation of barotropic current from the six current meter

TABLE 1. Amplitude and Greenwich Epoch of the eastward barotropic tidal current components for the north leg. The CRS model is the Cartwright et al. model.

Tidal constituent	Acoustic tomography	Schwiderski model	CRS model	Current meter (Luther)	Current meter (Dushaw)
			Amplitude (cm s^{-1})		
K_2	0.12 ± 0.04	—	0.14	0.10 ± 0.04	0.12 ± 0.02
S_2	0.53 ± 0.04	0.66	0.63	0.53 ± 0.05	0.60 ± 0.02
M_2	1.31 ± 0.03	1.28	1.42	1.32 ± 0.05	1.43 ± 0.02
N_2	0.14 ± 0.03	0.16	0.15	0.15 ± 0.05	0.19 ± 0.02
K_1	0.75 ± 0.04	0.45	0.53	0.74 ± 0.03	0.79 ± 0.02
P_1	0.18 ± 0.04	—	0.10	0.27 ± 0.02	0.30 ± 0.02
O_1	0.43 ± 0.03	0.33	0.38	0.46 ± 0.05	0.45 ± 0.02
Q_1	0.10 ± 0.03	—	0.05	0.07 ± 0.02	0.06 ± 0.02
			Greenwich phase (°G)		
K_2	268 ± 13	—	279	280 ± 21	268 ± 8
S_2	272 ± 4	270	276	280 ± 6	278 ± 2
M_2	223 ± 1	222	218	218 ± 2	214 ± 1
N_2	191 ± 13	184	201	216 ± 17	259 ± 7
K_1	128 ± 2	127	100	135 ± 3	142 ± 1
P_1	132 ± 11	—	129	141 ± 4	134 ± 4
O_1	101 ± 4	99	104	122 ± 7	117 ± 2
Q_1	64 ± 16	—	125	110 ± 14	103 ± 16

time series is somewhat subjective. Luther et al. (1991) estimated the barotropic current both by a weighted vertical average and by projecting the current meter data onto the appropriate dynamical vertical structure functions, with nearly identical results. To correct for stalling, Luther et al. (1991) found that the barotropic currents determined from the current meters required a scale factor correction (1.48 for zonal currents and 1.61 for meridional currents both included here) in order for them to agree with the low-frequency barotropic currents obtained from the Barotropic Electromagnetic and Pressure Experiment (BEMPEX) electrometer data. (The electromagnetic measurements cannot accurately determine the tides because of ionospheric noise and self-induction.) The harmonic constants were derived from the barotropic current by straightforward Fourier analysis. The error bars (90% confidence limit) for the current meter harmonic constants estimated by Luther et al. (1991) were found following appendix B of Munk and Cartwright (1966), with a modification to explicitly account for the uncertainties in the estimated noise variances.

We have recalculated the barotropic currents by inverting the current meter data for time series of barotropic and baroclinic mode amplitudes (the appendix and section 4), and then applying the inverse tidal analysis method described above to the resulting time series of barotropic current to derive the harmonic constants and their uncertainties. The baroclinic current is discussed in section 4c. The data from each current meter were first high-pass filtered by subtracting a 3-day running mean. The scale-factor corrections of Luther et al. (1991) were also applied. Different scale

factors are expected for different methods of analysis, which is the likely cause of the larger harmonic amplitudes in the weighted least squares case. The results are sensitive to the assumed noise levels for each current meter. Spectra show that the top two current meters are dominated by internal wave noise, while the bottom two current meters suffered stalls. Thus, the barotropic and baroclinic currents are essentially determined by the two current meters at depths of 946 and 2498 m.

Spectra of barotropic current derived in both ways show a large inertial peak, indicating that internal and inertial waves were aliased into the barotropic current. The amplitudes of the barotropic tidal harmonic constants can vary by as much as 30%, depending on the noise levels assumed for each current meter. The uncertainties for the derived harmonic constants do not take this subjectivity into account. The range and depth averaging inherent in the acoustic measurements results in barotropic tidal measurements that are as accurately determined from the 120-day record length of the tomographic measurements as from the year-long half-hourly current meter measurements.

c. Comparisons

Tables 1–3 show the results of the tidal analyses of the barotropic currents on each leg of the experiment triangle. The uncertainties (standard errors) in amplitude and phase were calculated by combining the weighted least squares estimates of the uncertainties of B_N and C_N according to (6), assuming Gaussian statistics. The amplitudes of Tables 1–3 include the lunar node factor (Schureman 1958) [the phase also is cor-

TABLE 2. Amplitude and Greenwich Epoch of the northward barotropic tidal current components for the east leg. The current meter constants should also be compared with the CRS model constants for meridional current on the north leg, since this comparison is for points that are nearby.

Tidal component	Acoustic tomography	Schwiderski model	CRS model	Current meter (Luther)	Current meter (Dushaw)	CRS model (North)
			Amplitude (cm s^{-1})			
K_2	0.15 ± 0.05	—	0.16	0.24 ± 0.03	0.16 ± 0.02	0.16
S_2	0.56 ± 0.05	0.61	0.60	0.52 ± 0.04	0.48 ± 0.02	0.61
M_2	1.54 ± 0.04	1.39	1.57	1.06 ± 0.05	1.18 ± 0.02	1.26
N_2	0.35 ± 0.04	0.23	0.29	0.27 ± 0.05	0.36 ± 0.02	0.23
K_1	0.41 ± 0.05	0.58	0.71	0.39 ± 0.02	0.41 ± 0.02	0.61
P_1	0.14 ± 0.05	—	0.19	0.13 ± 0.01	0.13 ± 0.02	0.19
O_1	0.25 ± 0.04	0.33	0.30	0.26 ± 0.02	0.25 ± 0.02	0.25
Q_1	0.06 ± 0.04	—	0.06	0.06 ± 0.01	0.06 ± 0.02	0.07
			Greenwich phase (°G)			
K_2	184 ± 16	—	199	199 ± 11	188 ± 6	207
S_2	207 ± 6	200	202	210 ± 5	205 ± 3	203
M_2	176 ± 2	177	172	170 ± 3	161 ± 1	173
N_2	169 ± 8	164	153	182 ± 10	202 ± 4	184
K_1	216 ± 7	230	240	229 ± 3	239 ± 3	249
P_1	229 ± 21	—	207	228 ± 6	231 ± 10	226
O_1	207 ± 9	215	229	227 ± 4	225 ± 5	222
Q_1	188 ± 34	—	205	208 ± 9	204 ± 19	168

rected for the lunar node through the use of Schureman's (1958) Table 15 to calculate Greenwich Epoch]. The tidal harmonic constants found from the acoustically determined currents agree with those found from current meters and with the Schwiderski and CRS tidal models. Nominal uncertainties for the CRS tidal model harmonic constants are 10% in amplitude and 6° in phase (D. Cartwright 1993, personal communication). (The CRS model derives tidal currents from the Schwiderski elevations.) Note that the current meter mooring was located roughly midway along the northern path of the experiment, a considerable distance from either of the other two paths. The comparison with these distant paths is still worthwhile because the barotropic tide wavelengths are large (Fig. 1). The longer range of the west leg of the experiment resulted in lower acoustical signal-to-noise ratio and thus a less reliable time series (some of the discrepancies in Table

TABLE 3. Amplitude and Greenwich Epoch of the northwestward barotropic tidal current components for the west leg.

Tidal component	Acoustic tomography	Schwiderski model	CRS model	Current meter (Luther)	Current meter (Dushaw)
			Amplitude (cm s^{-1})		
K_2	0.16 ± 0.08	—	0.18	0.12 ± 0.05	0.14 ± 0.02
S_2	0.33 ± 0.07	0.60	0.71	0.42 ± 0.05	0.44 ± 0.02
M_2	0.95 ± 0.07	0.94	1.05	0.68 ± 0.04	0.82 ± 0.02
N_2	0.16 ± 0.06	0.13	0.19	0.13 ± 0.05	0.24 ± 0.02
K_1	0.31 ± 0.07	0.53	0.68	0.58 ± 0.04	0.61 ± 0.02
P_1	0.07 ± 0.07	—	0.20	0.20 ± 0.02	0.22 ± 0.02
O_1	0.13 ± 0.06	0.35	0.35	0.40 ± 0.03	0.39 ± 0.02
Q_1	0.11 ± 0.06	—	0.07	0.07 ± 0.02	0.06 ± 0.02
			Greenwich phase (°G)		
K_2	143 ± 20	—	163	173 ± 28	155 ± 7
S_2	170 ± 14	160	169	158 ± 7	155 ± 3
M_2	131 ± 4	139	143	99 ± 4	104 ± 2
N_2	111 ± 23	146	147	165 ± 22	178 ± 6
K_1	306 ± 13	254	272	291 ± 4	290 ± 2
P_1	171 ± 61	—	309	285 ± 5	283 ± 6
O_1	255 ± 23	242	249	269 ± 4	266 ± 3
Q_1	217 ± 28	—	250	249 ± 18	236 ± 17

3 are likely due to this). The agreement between the various estimates of the harmonic constants was used by DWCHc to verify that tomographic techniques accurately determine barotropic currents.

The comparisons in Tables 1–3 complement the much more extensive comparison of tidal current measurements to the Schwiderski model by Luyten and Stommel (1991). They found that the M_2 tidal currents observed at 315 deep-sea locations generally agreed with those computed from the Schwiderski model. The comparison with the Schwiderski model was limited to the M_2 constituent because of the clarity of its signal, the inability to separate some of the tidal lines (S_2 and K_2, for example), and the lack of the tidal current harmonic constants of the Schwiderski model for other constituents. The good agreement of the acoustically determined harmonic constants with the model computations in this paper supports the accuracy of the empirical–numerical models. The model estimates for K_1 are less reliable than the rest, since near the 30°N critical latitude for this constituent the computation of tidal currents from the elevation can be inaccurate (D. Cartwright 1993, personal communication).

4. Baroclinic tides

a. Theory

The baroclinic tidal signal in the acoustic sum travel times and in the thermistor and current meter data is examined by extracting that part of the data consistent with the vertical structure of the internal tide. The displacement modes of the internal tide are given by solutions to the eigenvalue problem:

$$\frac{\partial^2}{\partial z^2} F(z) + q^2(N^2(z) - \omega^2)F(z) = 0 \quad (7a)$$

with the bottom boundary condition

$$F(D) = 0 \quad (7b)$$

and the free surface boundary condition

$$\frac{\partial}{\partial z} F(0) - gq^2 F(0) = 0, \quad (7c)$$

where q^2 is the eigenvalue, $N(z)$ is the buoyancy frequency, D is the ocean depth, and g is the gravitational acceleration. In (7), the buoyancy frequency is determined from CTD data collected in May and September 1987 during deployment and recovery of the acoustic moorings. The solutions to (7) are a linear superposition of a set of eigenfunctions, or modes, $F_n(z)$ with eigenvalues q_n^2. Here

$$q_n^2 = \frac{k_n^2}{\omega^2 - f^2}, \quad (8)$$

where k_n is the mode n wavenumber, ω is frequency, and f is the inertial frequency. The internal tides are

evanescent above the latitude where $\omega = f$; thus, the diurnal tides do not freely propagate above 30°N. Since $N^2 \gg \omega^2$, the frequency dependence of (7) can be ignored and the $F_n(z)$ are independent of ω. The displacement at frequency ω_p, where $\{\omega_p\}$ is the set of tidal constituent frequencies, is represented as

$$\zeta_p(\mathbf{x}, t) = \sum_{n=1}^{n=\infty} A_{pn} F_n(z) \exp i(\mathbf{x} \cdot \mathbf{k}_{pn} - \omega_p t + \phi_{pn}),$$

$$(9)$$

and the total internal tidal displacement is the sum of ζ_p over tidal frequencies. The frequencies ω_p and wavenumbers k_{pn} are given in Table 4, and A_{pn} (ϕ_{pn}) is the amplitude (phase) of the nth mode at frequency ω_p. The displacement modes $F_n(z)$ are normalized as

$$\int_D^0 F_n^2(z) N^2(z) dz = D\bar{N}^2, \quad (10)$$

where

$$\bar{N} = \frac{1}{D} \int_D^0 N(z) dz. \quad (11)$$

The temperature and sound-speed modes are obtained by multiplying the displacement modes by the potential temperature or sound speed gradient, respectively. Thus,

$$T_n(z) = -F_n(z) \frac{d\theta(z)}{dz} \quad (12)$$

and

$$C_n(z) = -F_n(z) \frac{dc_\theta(z)}{dz}, \quad (13)$$

where $\theta(z)$ is the potential temperature and $c_\theta(z)$ is the potential sound speed. Figure 2 shows the first two sound speed modes.

The baroclinic current modes are given by

TABLE 4. Properties of the internal tide modes from the eigenvalues of (8). The M_2 and S_2 constituents have frequencies (periods) 1.4053×10^{-4} rad s^{-1} (12.4206 h) and 1.4544×10^{-4} rad s^{-1} (12.0000 h), respectively. The phase speed is s, group speed is s_g, wavelength is λ, and wavenumber is k. These values were calculated using a buoyancy–frequency profile computed from the average of three CTD casts taken on the northern acoustic path in May 1987.

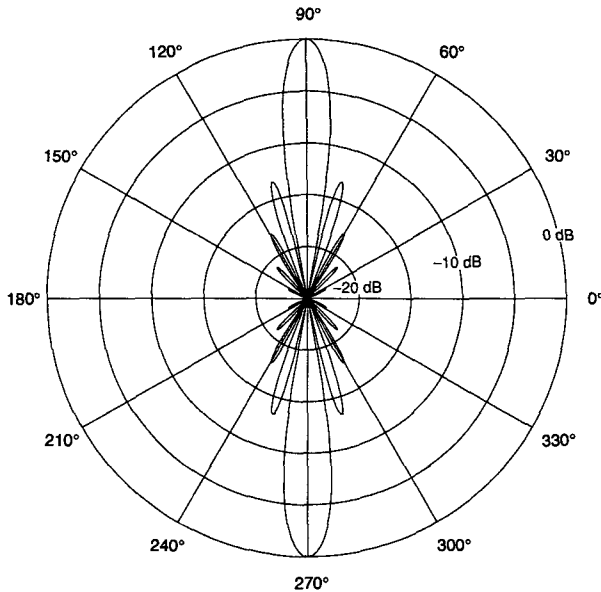| Mode	Constituent	s (m s^{-1})	s_g (m s^{-1})	λ (km)	k ($\times 10^{-2}$ rad km^{-1})
1	M_2	3.50	1.92	156	4.02
	S_2	3.41	1.97	147	4.27
2	M_2	1.70	0.94	76	8.26
	S_2	1.66	0.96	72	8.78
3	M_2	1.09	0.60	49	12.92
	S_2	1.06	0.61	46	13.73

FIG. 5. The beam pattern of a continuous line array of length 750 km with zonal orientation and 160-km incident wavelength. The units of the beam pattern are dB relative maximum (see Urick 1967). The antenna has the greatest response for wave propagation in the meridional direction. The acoustic array consists of three such line arrays with different orientations.

$$U_{pn}(z) = \left(\frac{\omega_p}{k_{pn}}\right)\frac{d}{dz} F_n(z). \qquad (14)$$

b. Acoustical observation

The high-frequency sum travel time data are a measure of the average perturbation of the sound speed field by the internal tide along the acoustic paths (the appendix). This is not to say that the internal tide is entirely independent of range on this path, rather that the travel times are range-averaged quantities with little horizontal resolution. The acoustic array acts as a three-component antenna for the incident internal tide field; the components are the line integrals along the three acoustic paths. Since the length of the line integral is much greater than the wavelength of the internal tide, the beam pattern is quite narrow (Urick 1967) (Fig. 5) and the antenna is highly directional. Further, since a significant part of the internal tide observed acoustically is phase locked over the 120-day record length (and the experiment is far from bottom relief that could generate an internal tide), the observed phase-locked internal tide must have a large (>1000 km?) coherence length. The short correlation length of order 100 km commonly assumed for the internal tide (Wunsch 1975) is not valid here, since it precludes the phase-locked observation.

Munk et al. (1981) suggested that the sound speed fluctuations caused by the tidal elevation (due to the pressure dependence of sound speed) would be ob-servable in the sum of reciprocal travel times, and hence the tidal elevation could be measured. (The change in travel time due to the lengthening of the acoustic path by elevation changes is negligible.) Using the M_2 elevation (Fig. 1) and assuming $\partial c/\partial z \approx 1.6 \times 10^{-2}$ m s^{-1}/m, a peak-to-peak travel time variation due to elevation is estimated to be about 4 ms. Comparing this value to the observed variations (Fig. 4) of about 20 (40) ms for the deep-turning (axial) rays shows that the pressure variations are small compared to the internal-tide sound speed fluctuations. In the absence of the internal tide signal, the measurement of the tidal elevation would be possible.

The sum travel times are inverted to obtain time series of mode amplitudes. The fit to the range-independent vertical modes of the internal tide accounts for about 60% of the high-pass filtered travel time variances on the north and west paths, while only 30%–40% of the variance of travel time data from the east path is accounted for by the range-independent model (Table 5). In the inversion it is assumed that the first-mode amplitude variance is 10 m^2, while that of the second mode is 1 m^2; thus, the first mode is weighted more heavily in the fit.

Using the tidal analysis technique described in the previous section, the phase-locked component of the first-mode amplitude time series is extracted (Table 6). The phase-locked (over the 120-day record length) tide accounts for 56% and 47% of the first-mode amplitude variance on the north and west paths, respectively, but only 18% of the variance on the east path. Simulated time series show that if the main variability were due to a narrowband internal tide, only 10%–15% of the first-mode amplitude variance would be accounted for by the phase-locked fit. On the north and west paths, the ratio of the M_2 and S_2 first-mode amplitudes is about the same as the ratio of the M_2 and S_2 barotropic tidal elevations.

Some fraction of the first-mode amplitude variance is due to tidal variability that is not phase locked and to internal wave noise. By including near-tidal frequencies in the weighted least squares procedure, it is estimated that about 15% of the first-mode amplitude variance is due to non-phase-locked tidal variability and the remaining 30% of the variance is due to internal wave noise (on the north and west paths). The internal wave noise in the mode amplitude time series results

TABLE 5. Comparison of modal composition of acoustic sum travel time data. Shown are the fractions in percent of the data variances that are accounted for by the baroclinic modes.

Rays	North	East	West
1–4	60	29	62
4–8	60	29	40
8–12	34	45	—
Axial	83	88	87

TABLE 6. Harmonic constants of the first mode baroclinic tide determined acoustically. The normalization of the modes is given by (11).

Tidal constituent	North	East	West
	Amplitude (m)		
K_2	0.7 ± 0.1	0.0 ± 0.1	0.1 ± 0.1
S_2	1.2 ± 0.1	0.5 ± 0.1	0.7 ± 0.1
M_2	2.4 ± 0.1	0.6 ± 0.1	1.3 ± 0.1
N_2	0.2 ± 0.1	0.0 ± 0.1	0.2 ± 0.1
K_1	0.1 ± 0.1	0.1 ± 0.1	0.1 ± 0.1
P_1	0.2 ± 0.1	0.1 ± 0.1	0.2 ± 0.1
O_1	0.1 ± 0.1	0.0 ± 0.1	0.2 ± 0.1
Q_1	0.0 ± 0.1	0.2 ± 0.1	0.1 ± 0.1
	Greenwich phase (°G)		
K_2	160 ± 12	277 ± 115	130 ± 51
S_2	200 ± 7	61 ± 12	101 ± 8
M_2	228 ± 3	47 ± 10	248 ± 4
N_2	42 ± 43	19 ± 120	143 ± 24
K_1	34 ± 95	281 ± 55	148 ± 58
P_1	221 ± 40	124 ± 69	231 ± 31
O_1	172 ± 53	131 ± 110	202 ± 28
Q_1	111 ± 268	42 ± 33	240 ± 66

from internal wave noise in the 13 ray travel times that is consistent with the vertical-mode structure (within the assumed noise levels of the travel times).

The higher-order internal tide modes are not evident in the data. A tidal analysis of the second-mode amplitude time series gives the same constituent phases as for the first mode; hence the second, and higher, modes are not separable from the first mode in the analysis. The vertical integration inherent in the acoustic measurements suppresses the higher modes, since the higher-order mode shapes have zero crossings. Further, the beam pattern for the much shorter wavelengths of the higher-order modes is much narrower than for the first mode. The physical presence of the higher-order modes is also less expected, since their shorter wavelengths cause faster dissipation than the first mode (LeBlond 1966; LeBlond and Mysak 1978).

Since the diurnal internal tide does not freely propagate above 30°N and no significant diurnal component was observed (Table 6), the observed semidiurnal internal tide must be of remote origin. If the observed internal tide were locally generated (from a nearby seamount, for example), then it is likely that an evanescent diurnal internal tide would be observed. Local generation of the internal tide by the barotropic tide is not likely since the K_1 barotropic tidal current is larger than that of S_2, for example, and no significant K_1 internal tide was observed.

The S_2 and M_2 phase difference on the north and west paths can be used to estimate the range to the region where the internal tide was generated (Hendry 1977). If the internal tide is generated with initial S_2 and M_2 phase difference $(G_{S_2} - G_{M_2})_0$, then

$$(k_{S_2} - k_{M_2})R = (G_{S_2} - G_{M_2}) - (G_{S_2} - G_{M_2})_0, \quad (15)$$

where R is the range, k_{S_2} and k_{M_2} are appropriate wavenumbers from Table 4, and $(G_{S_2} - G_{M_2}) + 360° = 332°$ is the phase difference for the north leg from Table 6. The initial phase difference is assumed to be the difference of the Schwiderski tidal elevation phases (Schwiderski 1979, 1981), which does not vary much between Hawaii ($+20°$) and the Aleutians ($+4°$). From (15), and using the tidal elevation phase differences at Hawaii, the range from the north (west) path to the internal tide origination region is about 2088 $\pm$ 53 km (1340 ± 62 km), where the uncertainty has been calculated using only the estimated phase uncertainties. If a northward propagating internal tide is assumed, then both these ranges suggest that the tide originated at about 22°–24°N. (The latitude for the western path has been calculated with respect to its midpoint.) This latitude and the absence of other significant bathymetric features at this distance suggests the internal tide originated at the Hawaiian Islands.

It is natural to consider some form of beam forming as a way to determine the orientation of the incident internal tide field. Beam forming using the amplitudes and phases of Table 6 could be attempted, but a significant difficulty is that the form of the incident wave is not known. The data are not consistent with a simple plane-wave model. A model that fits the data to within two or three standard deviations is an exponentially damped plane wave with a 420-km e-folding scale propagating 5° east of north. In this model the observed internal tide on the west leg is accounted for using the sidelobe of the beam pattern (Fig. 5), and the tidal amplitude increases greatly southward. It is likely that other solutions are possible (cylindrical spreading, for example).

The most robust approach may be to consider phases only and avoid the likely amplitude variation of the internal tide field. Assuming a general northward propagation, the difference between the M_2 (or S_2) phases on the north and west paths is given by

$$(G_{M_2}^{north} - G_{M_2}^{west}) = kX \cos\theta - 2n\pi, \quad (16)$$

where $n = 3$ is the number of wavelengths between the west and north leg midpoints, k is the wavenumber, X is the distance between the two midpoints, and θ is the direction of propagation (the two midpoints are at about the same longitude). Using the M_2 (S_2) phases, the direction of propagation found is 24° (16°) east of north (good to perhaps 10°–20°) (Fig. 6). This direction of propagation compares favorably with the approximate 20° slant of the Hawaiian Ridge and the constancy of the phase of the M_2 (and S_2) barotropic elevation (Schwiderski 1979 and 1981) along the Hawaiian Ridge (Fig. 1), though this result must remain speculative. Indeed, given the narrow beam pattern of the integral measurements, the north and west legs may be measuring two separate components of an internal wave field made up of a continuum of components.
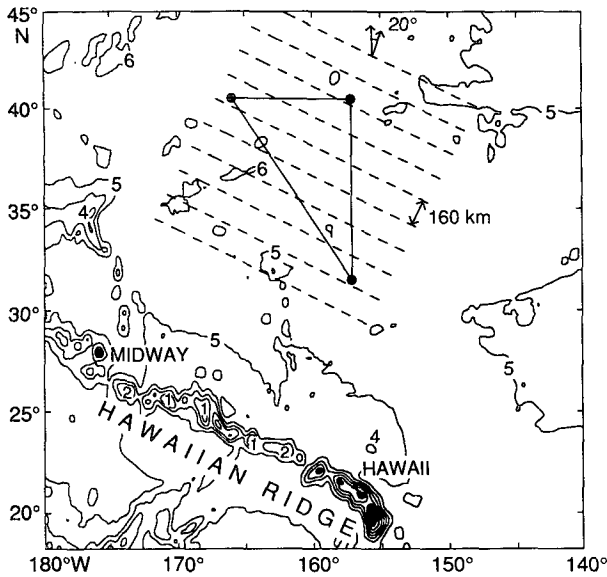
FIG. 6. Schematic diagram showing the relation of the hypothesized internal tide field to the acoustic array. The depths are shown in kilometers, and the dashed lines represent the crests of a wave with 160-km wavelength.

c. Thermistor and current meter observations

The moored thermistors and current meters provide another, albeit noisy, view of the internal tide. The point measurements do not provide the spatial filtering provided by the acoustic measurements, so all internal tide (and internal wave) wavelengths contribute equally. The point measurements have no directionality. By examining the phase-locked component; however, the shorter-scale, randomly phased signals can be filtered to some degree.

1) THERMISTOR DATA

After high-pass filtering the time series with a 2-day running mean, the first two internal-tide temperature modes were fit to data from the top four thermistors, giving a time series of mode amplitudes (see the appendix for the procedure). Spectra of these data show that only the thermistors at 296 and 946 m have significant tidal peaks; the second mode is therefore essentially unresolved. As in the case of the analysis of the current meter data, the solutions for the mode amplitudes are somewhat subjective, depending on the noise levels assumed for each thermistor. The tidal harmonic constants, discussed next, are reasonably robust to changes in weighting, however. Table 7 shows the quality of the modal fit to the data.

The phase-locked component of the first-mode amplitude time series was found using the same inverse method used for the acoustic data. Table 8 gives the harmonic constants for the year-long time series. While the deterministic component accounted for 56% of the

TABLE 7. Comparison of modal composition of thermistor and current meter data. Shown are the fractions in percent of the data variances that are accounted for by five baroclinic modes (and the barotropic mode in the case of the current meters) but with the first mode heavily weighted: T is temperature, U is eastward current, and V is northward current.

Depth (m)	T	U	V
73	1	3	8
173	5	16	10
296	69	—	—
946	90	95	97
2498	—	42	66
5650	—	7	6
5722	—	33	15

acoustically determined mode amplitude time-series variance, it accounts for only 9% of the thermistor-determined time-series variance. The diurnal amplitudes are zero within uncertainty. The harmonic amplitudes vary by 30%–40% with changes to the assumed thermistor noise levels and a priori mode amplitude weights, but the harmonic phases vary by only a few degrees. As was the case for the current meter results, the derived uncertainties for the harmonic constants do not take into account the subjectivity of the mode amplitude determination.

The M_2 and S_2 harmonic constants reasonably agree with the acoustic results for the north path, and in both cases the M_2 phase leads the S_2 phase. As will be further discussed below, these results are consistent with the northward propagating internal-tide model.

TABLE 8. Harmonic constants of the first-mode baroclinic tide determined from year-long moored thermistor and current meter data: T is temperature, U is eastward current, and V is northward current. The normalization of the modes is given by (11).

Tidal constituent	T	U	V
	Amplitude (m)		
K_2	0.1 ± 0.1	0.9 ± 0.1	1.0 ± 0.1
S_2	0.9 ± 0.1	1.3 ± 0.1	1.7 ± 0.1
M_2	3.1 ± 0.1	1.9 ± 0.1	4.1 ± 0.1
N_2	0.6 ± 0.1	1.1 ± 0.1	1.7 ± 0.1
K_1	0.3 ± 0.1	0.6 ± 0.1	0.1 ± 0.1
P_1	0.1 ± 0.1	0.1 ± 0.1	0.0 ± 0.1
O_1	0.1 ± 0.1	0.3 ± 0.1	0.3 ± 0.1
Q_1	0.1 ± 0.1	0.0 ± 0.1	0.1 ± 0.1
	Greenwich phase (°G)		
K_2	262 ± 44	128 ± 5	40 ± 6
S_2	245 ± 7	106 ± 3	54 ± 4
M_2	184 ± 2	295 ± 2	199 ± 1
N_2	69 ± 11	126 ± 4	33 ± 4
K_1	13 ± 22	331 ± 7	20 ± 38
P_1	38 ± 43	346 ± 44	83 ± 195
O_1	346 ± 46	303 ± 14	84 ± 23
Q_1	87 ± 84	342 ± 126	295 ± 109

2) CURRENT METER DATA

The current meter data were inverted to obtain year-long time series of barotropic and baroclinic mode amplitudes, as described in section 3. The harmonic constants for the internal tide current were found from the time series of the amplitude of the first current mode (Table 8). The mode amplitudes are somewhat sensitive to the assumptions, but the results for the harmonic constants are robust to 30%–40% in amplitude and to a few degrees in phase. The phase-locked component accounts for about 10% of the meridional and zonal first-mode amplitude time-series variance. (The current meter data has been high-pass filtered, as described in section 3.)

To examine the stability of the harmonic constants over time, the harmonic constants were determined from independent 100-day-long sections of the first-mode amplitude time series. The amplitude of the M_2 constituent, determined from the zonal and meridional current and from temperature, varied by up to 40% between data sections; the phases varied by about 20°. The S_2 harmonic constants varied considerably. This instability of the harmonic constants derived from the point measurements is not unexpected, given the weak signal-to-noise ratio and subjectivity of the analysis, but could also be caused by natural random variability of the local internal tide.

The M_2 amplitude and phase of the first mode calculated from the meridional current (4.1 m, 199° G) are consistent with the thermistor result (3.1 m, 184° G), but the first mode from the zonal current has a weaker amplitude (1.9 m, 295° G) and appears to lead the meridional first mode by about 100°. Levine and Richman (1989) describe a technique for determining the internal tide propagation direction by rewriting the zonal and meridional currents into clockwise and anticlockwise components. The direction of propagation is taken as the direction that maximizes the clockwise polarization, though there is a 180° ambiguity. Applying this technique to the M_2 harmonic constants shows that the maximum clockwise polarization occurs for meridional propagation. The major axis of the tidal elipse is also meridionally oriented. The 180° ambiguity can be resolved by using the displacement phase. For a northward propagating internal tide (Hendry 1977),

$$\zeta(z, t) = AF(z) \cos(\omega t - ky - G_A), \quad (17a)$$

$$u(z, t) = A\left(\frac{f}{\omega}\right) U(z) \cos\left[\omega t - ky - \left(G_A + \frac{\pi}{2}\right)\right], \quad (17b)$$

and

$$v(z, t) = AU(z) \cos(\omega t - ky - G_A), \quad (17c)$$

where ζ is the displacement, u is the zonal current, v is the meridional current, A is the amplitude, G_A is the

phase, and $F(z)$ and $U(z)$ are defined by (7), (10), and (14). For a northward propagating internal tide, the amplitude and phase of the displacement and meridional current are expected to be the same, while the amplitude of the zonal current is reduced by a factor of $f/\omega = 0.67$ and the phase leads the displacement phase by $\pi/2$. Within the uncertainty caused by the sensitivity to the assumed noise levels, the results for the M_2 harmonic constants in Table 8 are consistent with (17), as well as the acoustical result for the average displacement along the north path (2.4 m, 228° G).

In Table 8, the S_2 harmonic constants are not consistent with the northward propagating internal tide model, due to the weaker S_2 signal to noise. The observed S_2 amplitudes are about 1 m, but in Table 8 they are comparable to the K_2 and N_2 amplitudes. In the phase-locked case the K_2 and N_2 amplitudes could be expected to be reduced relative to the S_2 amplitude as occurs in the barotropic tide and in the acoustical observations of the internal tide (Table 6). Thus, the uncertainty due to the background internal-tide noise in the point measurements appears to be about 1 m, which is consistent with the differences between the harmonic amplitudes determined from the 100-day-long sections of data. The calculated error bars are smaller than the actual 1-m uncertainty because the noise in the harmonic analysis is assumed to be white, which is not the case when the noise is the non-phase-locked component of the internal tide signal in the point measurements.

d. Effect of the baroclinic current on estimation of the barotropic current

The effect of the internal tide currents on the barotropic tidal harmonic constants determined acoustically can be estimated using (17b) and the displacement harmonic constants for the internal tide from Table 6. The false barotropic current signal due to the M_2 internal tide current has an amplitude of 0.05 (0.29) cm s^{-1} and a 129° (309°) phase for the deep-turning (axial) ray travel times. (Note that the first mode internal tide has a zero crossing. The depth average of this mode, appropriate for the deep-turning rays, is of opposite sign from the value of the mode at 700 m, appropriate for the axial ray.) These values, when added to the M_2 barotropic current harmonic constants in Table 1, show that the internal tide affects the deep-turning (axial) ray current measurement by less than 0.01 (0.05) cm s^{-1} in amplitude and about 2° (10°) in phase. Since the barotropic current is estimated using 12 deep-turning rays and only one axial ray, we conclude that the internal tide affects the barotropic current harmonic constants by an amount less than the uncertainty.

5. Tidal energy

The acoustically determined first baroclinic mode amplitudes can be used to estimate the large-scale

baroclinic tidal energy, and thus the ratio of baroclinic to barotropic tidal energy can be determined. Using these amplitudes grossly underestimates the total internal tide energy, however, since the acoustic measurements give a range average, while the average of the squared perturbation is required to determine the total energy. The energy content of the shorter-scale internal tides is lost in the range average so that the energy determined acoustically is a lower bound on the internal-tide energy. Further, the acoustic data are sensitive only to energy propagating in a narrow range of directions, and considerable anisotropy in the internal tide field is apparent. The estimated energy is restricted to the estimated tidal component (70% of the variance) to eliminate apparent internal wave noise. The calculations here are for the measurements on the north path because this path may have been along crests of the internal tide and because these results can be compared with results from the current meter and thermistor data.

The displacement of the isopycnals is given by (9). With the displacement determined from the time series of mode amplitudes, the potential energy (not averaged over a tidal period) of all constituents is

$$PE(t) = \frac{1}{2} \int_D^0 \rho(z) N^2(z) \zeta^2(z, t) dz. \quad (18)$$

The time average of potential energy so determined, and corrected for internal wave contamination, is 26 J m^{-2}. Since the ratio of potential energy to kinetic energy is to good approximation $(\omega^2 - f^2)/(\omega^2 + f^2)$ = 0.38 (Wunsch 1975), the kinetic energy follows directly and is about 69 J m^{-2}. Thus, the net internal tidal energy observed acoustically is about 95 J m^{-2}. The time-averaged potential energy at the M$_2$ frequency is 14 J m^{-2}, giving a kinetic energy of 37 J m^{-2} and a total energy of 51 J m^{-2}.

The internal tide potential and kinetic energies were calculated using the first-mode amplitudes derived from the thermistor and current meter data. The potential energy in the semidiurnal band was 65 J m^{-2}, while the potential energy within $\pm 1/100$ cpd of the M$_2$ frequency was 52 J m^{-2}. The kinetic energy in the semidiurnal band was 250 J m^{-2}, with 150 J m^{-2} within $\pm 1/100$ cpd of the M$_2$ frequency. Thus, the net energy is about 315 J m^{-2}, with about 200 J m^{-2} in the M$_2$ band. In all of these values, the uncertainty due to the background internal-wave variability is about 15%. The measured ratio of potential to kinetic energy is about 0.26 (0.35) in the semidiurnal (M$_2$) frequencies, which compares reasonably well with the theoretical value. The energy inferred from the thermistor and current meter data is about three times the energy inferred from the range-averaging acoustic data.

The barotropic tidal energy is

$$E(t) = \frac{1}{2} \rho g \eta^2(t) + \frac{1}{2} \rho D(U^2(t) + V^2(t)), \quad (19)$$

where these terms are the potential and kinetic energies, respectively. The tidal elevation $\eta(t)$ is determined here from the Schwiderski (1980) model, and the zonal (U) and meridional (V) currents are given by the acoustical estimates. The time average of the barotropic tidal energy is about 1200 J m^{-2}, which, using the range-averaged case, gives a lower limit for the ratio of baroclinic to barotropic tidal energy of about 8%. The ratio using the internal tide energy determined at one point is 26%. These values can be compared with those reported by Wunsch, which were typically 10%–50% (Wunsch 1975; Hendershott 1981).

Hendry (1977) estimated the energy flux of the first-mode internal tide in the MODE region to be 300 W m^{-1}. Hendry used a simplified model of internal tide generation (Rattray et al. 1969) to show that interaction of the barotropic tidal current with the Blake Escarpment, the likely origin of the observed deterministic internal tide in MODE, could generate an energy flux of about 400 W m^{-1} in the M$_2$ first baroclinic mode. The internal tide energy flux, which is the product of energy density and the group speed, inferred from our acoustic measurements is about 180 W m^{-1}. The simplified model used by Hendry, applied to the circumstances of the Hawaiian Ridge, shows that the acoustically derived energy flux can be reasonably accounted for by generation at the Hawaiian Ridge.

6. Predicted travel time noise due to internal waves

The observed variance in the travel times due to internal waves is defined as the variance remaining after the modal signature has been removed (Table 9). This definition assumes that not all of the internal tide is deterministic and that the internal tide will affect the travel times in a way consistent with the modal structure. Some internal wave noise will leak into the modal

TABLE 9. The detided, high-frequency (>1 cpd) travel time variances. If T^+ and T^- are uncorrelated, the variances of $(T^+ + T^-)$ and $(T^+ - T^-)$ would equal twice the one-way variances. The one-way travel time variances have been calculated from the sum and the difference variances, since it is difficult to remove the tidal signals from the one-way variances.

		$\langle T^2 \rangle$ (ms^2)	$\frac{1}{2} \langle (T^+ + T^-)^2 \rangle$ (ms^2)	$\frac{1}{2} \langle (T^+ - T^-)^2 \rangle$ (ms^2)
North	Rays 1–4	8	12	3
	Rays 5–8	13	19	6
	Rays 9–12	38	60	15
	Axial	58	75	41
East	Rays 2, 4	15	22	7
	Rays 5–8	23	32	13
	Rays 9–12	45	69	21
	Axial	45	38	52
West	Rays 1, 2, 4	17	27	7
	Rays 5, 6, 7	39	67	10
	Axial	88	99	77

fit, but complete separation of the internal wave and internal tide variances can never be achieved. The predicted travel time variance due to internal waves (Flatté and Stoughton 1988) is very sensitive to whether or not the ray paths reflect from the surface. If a Garrett–Munk spectrum is assumed, then the predicted internal wave variance for rays that reflect from the surface is about 5 ms^2, while for rays that turn just below the surface, the prediction is about 50 ms^2 (S. M. Flatté 1993, personal communication). The observed variances are roughly consistent with this result in that the earliest arriving rays, which are strongly surface reflecting, have lower variances than the latest arriving rays. The latest arriving, deep-turning ray travel times are also less consistent with the internal tide vertical modes (Table 5, rays 8–12), as expected given their greater internal-wave noise. Our observed variances for shallow-turning (upper turning point) rays are intermediate between the predictions for surface-reflecting and shallow-turning rays, however. The range dependence of the sound speed field of this experiment may result in ray paths that reflect from the surface at some upper turning points and not at others. Our results are thus consistent with internal wave effects, but cannot be quantitatively compared because of sensitivity to the exact structure of the range-dependent ocean sound channel. Predictions for individual rays near the axis are all in the range from 35 to 55 ms^2, which is consistent with the observed axial-ray, travel time variance.

7. Discussion

The acoustical observation of the tide is range and depth averaging, which suppresses internal wave noise and provides better estimates of both the barotropic tide and the deterministic part of the internal tide signal than moored thermistor and current meter observations. Barotropic tidal harmonic constants and their uncertainties determined from a nonuniformly sampled acoustic travel-time time series using a weighted least squares estimation procedure agree within uncertainty with those determined from the Schwiderski and the Cartwright, Ray, and Sanchez tidal empirical–numerical models, verifying both the acoustic measurements and the models. A significant, phase-locked internal tide component, which appears to have been generated at the Hawaiian Ridge, is found. The hypothesis that the acoustically observed internal tide originates from the Hawaiian Ridge with crests aligned approximately along the north acoustic path is supported by i) the anisotropy of the internal tide field as indicated by the strength of the tidal signal on the north and west paths and the weakness of the tidal signal on the east path; ii) the agreement between the M_2 harmonic constants on the north path determined by the acoustics, thermistors, and current meters; iii) the deterministic nature of the tidal signal (insofar as the stability of the tidal constituent phases in time implies

that the internal tide has a large horizontal coherence length); iv) the range to the Hawaiian Ridge as determined by the M_2 and S_2 phase differences; and v) the apparent northward propagation observed by the thermistors and current meters. While the point-to-point correlation of the internal-tide field apparently decays with an O(100 km) length scale due to the dominant narrowband processes, the large-scale coherence of the internal tide implies a long oscillatory tail.

The large internal tide amplitude observed at the Hawaiian Ocean Time Series (HOTS) site located about 100 km north of Oahu lends additional credence to the Hawaiian origin of the acoustically observed internal tide. Chiswell (1994) reported a typical peak-to-peak displacement of the semidiurnal internal tide of about 25 m at the HOTS site, and the vertical structure was dominated by the second or third mode. (Chiswell's paper is the only reported observation of the internal tide near Hawaii known to the authors.) Chiswell's analysis was limited by the data to the top kilometer. A comparable peak-to-peak displacement inferred from the acoustical data is about 5–6 m at depths between 1 and 3 km (or peak-to-peak temperature variations of about 40 m °C at 400 m). The internal tide field near the Hawaiian Ridge is likely to be a complicated field generated by numerous point sources, and the extent to which the HOTS observations can be applied to the entire Hawaiian Ridge is unknown.

A speculative picture of the life cycle of the internal tide generated at Hawaii can be drawn. The internal tide is likely to be generated along the Hawaiian Ridge with greatly varying amplitude and modal composition but with the approximate constant phase of the barotropic tide. Rattray et al.'s (1969) model of internal tide generation predicts for a constant buoyancy frequency that the maximum excitation of the first mode occurs when the shelf depth is half the ocean depth (Hendry 1977), which is the approximate case for much of the Hawaiian Ridge. Thus, the first mode can be expected to be a significant component of the internal tide. As the tide propagates northward, apparently linearly, theory (LeBlond 1966; Schott 1977; LeBlond and Mysak 1978) suggests that the higher-order modes dissipate, leaving only the first mode, and the waves from the individual point or segment sources merge to form a large-scale wave front. Linear propagation is possible because the currents and eddy energy are weak in this region. At 2000-km range the first mode has traveled 13–14 periods (about 6 days), less than an expected decay time (for a vertical eddy coefficient of 10^3 cm^2 s^{-1}) of about 20 periods (LeBlond 1966; Schott 1977).

Barnett and Bernstein (1975) examined moored thermistor data collected between 41° and 44°N, just north of our acoustic array, in order to assess the horizontal scales of midocean internal tides. They found

that the thermobaric energy associated with the semi-diurnal tide showed no coherence in either the vertical (0–150 m) or horizontal (5–500 km). There are two possible reasons for the disagreement between their conclusions and our observations. First, the deepest thermistors available to them were at 150 m, while the discussion here has shown that internal wave variability dominates the tidal signals above 200–300 m (Table 7). Second, the horizontal averaging inherent in the acoustic measurements provides a distinct advantage in detecting large-scale signals.

Headrick et al. (1993) reported tidal travel time variability on 3000–4000-km-long transmissions in the Pacific. On two of five paths, they found significant disagreement with modeled barotropic tidal currents. They attribute the disagreement to a deterministic baroclinic tidal signal, generated at seamounts near the acoustic paths. Given the results found here, the observed disagreement might also be due to a far-field internal tide.

The ratio of baroclinic to barotropic tidal energy in the range-averaged case is about 8%, while a ratio of 26% was observed at one point. The range-averaged determination represents a lower bound because of the spatial filtering and angular sensitivity inherent in the measurements. The tidal energy flux was estimated to be about 180 W m^{-1}, apparently northward. The observed energy, presumably dissipated at distant shores, accounts for only a small fraction of the total tidal dissipation of 3×10^{12} W (Wunsch 1975). Acoustical observations of the internal tide at increasing range from Hawaii could be used to determine the tidal attenuation rate (and a vertical eddy diffusivity) (Le-Blond 1966). Sjoberg and Stigebrandt (1992) have numerically computed the geographical distribution of the energy flux to mixing processes originating from topographic generation of the internal tide. They arbitrarily assumed that the generated internal tide energy was dissipated within 100 km. When combined with internal tide measurements at Hawaii, the present data could provide information on the horizontal dissipation scales that is presently lacking.

APPENDIX

The Modal Decomposition of Data and the Determination of Tidal Harmonic Constants

This appendix gives a brief summary of the inverse method used to determine the tidal harmonic constants and their uncertainty and to decompose the moored temperature and acoustic travel time data into vertical modes. The basic form of the inverse problem is

$$d_i = \sum_j G_{ij}A_j + \epsilon_i, \qquad (A1)$$

where d_i are the data, G_{ij} is the matrix that defines the forward problem, ϵ_i is noise, and A_j are the tidal harmonic constants or mode amplitudes. The forward problems for the tidal and modal fits will be discussed in turn.

a. Determination of tidal harmonic constants

For determining the tidal harmonic constants, the data d_i are the time series of barotropic current or baroclinic mode amplitudes. The noise ϵ_i is defined as the rms of that part of the time series that is not due to tides. The noise is assumed to be approximately white. From (5),

$$G_{ij} = \cos\omega_j t_i \quad \text{or} \quad \sin\omega_j t_i, \qquad (A2)$$

and once the A_j [which are the set $\{B_N, C_N\}$ of (5)] and their uncertainties are found, the harmonic constants and their uncertainties can be found from (6).

b. Acoustic determination of mode amplitudes

The internal tide mode amplitudes are determined from the high-frequency sum travel times, which are the data d_i. The noise is defined, as for the tides, as the rms of that part of the travel-time time series that is not consistent with the vertical mode structure. The noise is mainly due to internal wave variability. The sound speed variability is modeled as

$$\delta c(z, t) = \sum_{j=1}^{\infty} A_j(t)C_j(z), \qquad (A3)$$

where $C_j(z)$ is the jth baroclinic-tide sound speed mode defined by (13). Since the travel times used are high-pass filtered, T_{0i} is removed from (2) and the matrix G_{ij} is

$$G_{ij} = -2 \int_{\Gamma_i} \frac{C_j(z)}{c_0^2(x, t)} \, ds. \qquad (A4)$$

c. Thermistor (and current meter) determination of mode amplitudes

To solve for the internal tide mode amplitudes from the thermistor data, the data are the high-pass filtered

temperature recorded by each thermistor. The noise is defined by iteration as for the acoustic problem. The noise is mainly due to internal wave variability. The temperature variability is modeled as

$$\delta T(z, t) = \sum_{j=1}^{\infty} A_j(t) T_j(z), \quad (A5)$$

where $T_j(z)$ is the jth baroclinic-tide temperature mode defined by (12). The matrix G_{ij} is

$$G_{ij} = T_j(z_i), \quad (A6)$$

where z_i is the depth of the ith thermistor. Application of the inverse to the current meter data uses a similar forward problem, with the temperature modes replaced by a barotropic (depth independent) mode and baroclinic current modes.

d. Inversions

Inverse theory provides a solution for the A_j from the d_i (Aki and Richards 1980). One requires an a priori model covariance matrix $(\mathbf{R}_{AA})_{jj} = \langle (A_j)^2 \rangle$ (assumed diagonal) and an a priori data noise covariance matrix $(\mathbf{R}_{\epsilon\epsilon})_{ii} = \langle (\epsilon_i)^2 \rangle$ (also assumed diagonal). In general, $\epsilon_i \neq \epsilon_j$ for $i \neq j$. Then, using matrix notation,

$$\mathbf{R}_{dd} = \mathbf{G}\mathbf{R}_{AA}\mathbf{G}^T + \mathbf{R}_{\epsilon\epsilon} \quad (A7)$$

and

$$\mathbf{L} = \mathbf{R}_{AA}\mathbf{G}^T\mathbf{R}_{dd}^{-1} \quad (A8)$$

or, equivalently,

$$\mathbf{L} = (\mathbf{G}^T\mathbf{R}_{\epsilon\epsilon}^{-1}\mathbf{G} + \mathbf{R}_{AA}^{-1})^{-1}\mathbf{G}^T\mathbf{R}_{\epsilon\epsilon}^{-1}. \quad (A9)$$

Here $\mathbf{L}$ is the inverse operator particular to the choice of ocean model and a priori variances. The model solution is

$$\hat{\mathbf{A}} = \mathbf{L}\mathbf{d}, \quad (A10)$$

where $\mathbf{d}$ is a column vector. The model error covariance matrix is

$$\mathbf{E} = \mathbf{R}_{AA} - \mathbf{L}\mathbf{G}\mathbf{R}_{AA}. \quad (A11)$$

The uncertainties of the A_j values are given by the square root of the diagonal of $\mathbf{E}$, though sometimes the off-diagonal elements are important; $\mathbf{L}\mathbf{G}$ is the resolution matrix: $\hat{\mathbf{A}} = \mathbf{L}\mathbf{G}\mathbf{A}$, where $\mathbf{A}$ is the "true" solution for the A_j values.

The major difficulty with the solution $\hat{\mathbf{A}}$ is that it is sometimes sensitive to the choice of ocean model and assumed a priori variances, though such sensitivity often reflects a large uncertainty in the solution.

If $\mathbf{R}_{AA}$ is infinite and $R_{\epsilon\epsilon}$ is a constant, the inverse technique reduces to unweighted least squares (the generalized inverse), with solution

$$\hat{\mathbf{A}} = (\mathbf{G}^T\mathbf{G})^{-1}\mathbf{G}^T\mathbf{d}. \quad (A12)$$

REFERENCES

Aki, K., and P. G. Richards, 1980: *Quantitative Seismology: Theory and Methods.* Vol. 2. W. H. Freeman, 932 pp.

Barnett, T. P., and R. L. Bernstein, 1975: Horizontal scales of midocean internal tides. *J. Geophys. Res.,* **80,** 1962–1964.

Cartwright, D. E., R. D. Ray, and B. V. Sanchez, 1992: A computer program for predicting oceanic tidal currents. NASA Tech. Memo. 104578, Goddard Space Flight Center, Greenbelt, MD, 21 pp.

Chiswell, S. M., 1994: Vertical structure of the baroclinic tides in the central North Pacific subtropical gyre. *J. Phys. Oceanogr.,* **24,** 2032–2039.

Dushaw, B. D., P. F. Worcester, B. D. Cornuelle, and B. M. Howe, 1993a: On equations for the speed of sound in seawater. *J. Acoust. Soc. Amer.,* **93,** 255–275.

——, ——, ——, and ——, 1993b: Variability of heat content in the Central North Pacific in summer 1987 determined from long-range acoustic transmissions. *J. Phys. Oceanogr.,* **23,** 2650–2666.

——, ——, and ——, 1994: Barotropic currents and vorticity in the central North Pacific Ocean during summer 1987 determined from long-range reciprocal acoustic transmissions. *J. Geophys. Res.,* **99,** 3263–3272.

Emery, W. J., 1983: On the geographical variability of the upper level mean and eddy fields in the North Atlantic and North Pacific. *J. Phys. Oceanogr.,* **13,** 269–291.

Flatté, S. M., and R. B. Stoughton, 1988: Predictions of internal-wave effects on ocean acoustic coherence, travel time variance, and intensity moments for very long-range propagation. *J. Acoust. Soc. Amer.,* **84,** 1414–1424.

Headrick, R. H., J. L. Spiesberger, and P. J. Bushong, 1993: Tidal signals in basin-scale acoustic transmissions. *J. Acoust. Soc. Amer.,* **93,** 790–802.

Hendershott, M. C., 1981: Long waves and ocean tides. *Evolution of Physical Oceanography,* B. A. Warren and C. Wunsch, Eds., The MIT Press, 292–341.

Hendry, R. M., 1977: Observations of the semidiurnal internal tide in the western North Atlantic ocean. *Philos. Trans. Roy. Soc. London,* **A286,** 1–24.

Howe, B. M., P. F. Worcester, and R. C. Spindel, 1987: Ocean acoustic tomography: Mesoscale velocity. *J. Geophys. Res.,* **92,** 3785–3805.

LeBlond, P. H., 1966: On the damping of internal gravity waves in a continuously stratified ocean. *J. Fluid Mech.,* **25,** 121–142.

——, and L. A. Mysak, 1978: *Waves in the Ocean.* Elsevier, 602 pp.

Levine, M. D., and J. G. Richman, 1989: Extracting the internal tide from data: methods and observations from the Mixed Layer Dynamics Experiment. *J. Geophys. Res.,* **94,** 8125–8134.

Luther, D. S., J. H. Filloux, and A. D. Chave, 1991: Low-frequency, motionally induced electromagnetic fields in the ocean 2: Electric field and Eulerian current comparison. *J. Geophys. Res.,* **96,** 12 797–12 814.

Luyten, J. R., and H. M. Stommel, 1991: Comparison of M_2 tidal currents observed by some deep moored current meters with those of the Schwiderski and Laplace models. *Deep-Sea Res.,* **38,** S573–S589.

Munk, W., and K. Hasselmann, 1964: Super-resolution of tides. *Studies on Oceanography,* University of Tokyo Press, 339–344.

——, and D. E. Cartwright, 1966: Tidal spectroscopy and prediction. *Philos. Trans. Roy. Soc. London,* **A259,** 533–581.

——, B. Zetler, J. Clark, S. Gill, D. Porter, J. Spiesberger, and R. Spindel, 1981: Tidal effects on long-range sound transmission. *J. Geophys. Res.,* **86,** 6399–6410.

Perkins, H., T. J. Sherwin, and T. S. Hopkins, 1994: Amplification of tidal currents by overflow on the Iceland–Faeroe Ridge. *J. Phys. Oceanogr.,* **24,** 721–735.

Pugh, D. T., 1987: *Tides, Surges and Mean Sea-Level.* John Wiley and Sons, 472 pp.

Rattray, M., Jr., J. G. Dworski, and P. E. Kovala, 1969: Generation of long internal waves at the continental slope. *Deep-Sea Res.,* **16** (Suppl.), 179–195.

Schott, F., 1977: On the energetics of baroclinic tides in the North Atlantic. *Ann. Geophys.,* **33,** 41–62.

Schureman, P., 1958: Manual of harmonic analysis and prediction of tides. Spec. Publ. 98, U.S. Govt. Printing Office, 317 pp.

Schwiderski, E. W., 1979: Global ocean tides, Part II: The semidiurnal principal lunar tide (M2), atlas of tidal charts and maps. Naval Surface Weapons Center, Tech. Rep. 79-414, Dahlgren, VA, 87 pp.

——, 1980: Ocean tides. Part I: Global tide equations. Part II: A hydrodynamical interpolation model. *Mar. Geod.,* **3,** 161–125.

——, 1981: Global ocean tides, Part III: The semidiurnal principal solar tide (S2), atlas of tidal charts and maps. Naval Surface Weapons Center, Tech. Rep. 81-122, Dahlgren, VA, 96 pp.

Shum, C. K., R. A. Werner, D. T. Sandwell, B. H. Zhang, R. S. Nerem, and B. D. Tapley, 1990: Variations of global mesoscale eddy energy observed from Geosat. *J. Geophys. Res.,* **95,** 17 865–17 876.

Sjoberg, B., and A. Stigebrandt, 1992: Computations of the geographical distribution of the energy flux to mixing processes via internal tides and the associated vertical circulation in the ocean. *Deep-Sea Res.,* **39,** 269–291.

Urick, R. J., 1967: *Principles of Underwater Sound for Engineers.* McGraw-Hill, 342 pp.

Weinberg, N. L., J. G. Clark, and R. P. Flanagan, 1974: Internal tidal influence on deep-ocean acoustic-ray propagation. *J. Acoust. Soc.,* **56,** 447–458.

Worcester, P. F., B. D. Dushaw, and B. M. Howe, 1990: Gyre-scale current measurements using reciprocal acoustic transmissions. *Proc. Fourth IEEE Working Conf. on Current Measurement,* Clinton, MD, IEEE, 65–70.

——, ——, and ——, 1991: Gyre-scale reciprocal acoustic transmissions. *Ocean Variability and Acoustic Propagation,* J. Potter and A. Warn-Varnas, Eds., Kluwer Academic, 119–134.

Wunsch, C., 1975: Internal tides in the ocean. *Rev. Geophys. Space Phys.,* **13,** 167–182.

Zetler, B. D., M. D. Schuldt, R. W. Whipple, and S. D. Hicks, 1965: Harmonic analysis of tides from data randomly spaced in time. *J. Geophys. Res.,* **70,** 2805–2811.